UC Davis
UC Davis Previously Published Works

Title

Decoding diffuse light scattering dynamics in layered tissues: path length versus fluctuation time scale.

Permalink

Journal

ISSN

Authors

Aparanji, Santosh

Zhao, Mingjun

Srinivasan, Vivek J

Publication Date

DOI

Decoding diffuse light scattering dynamics in layered tissues: path length versus fluctuation time scale

Santosh Aparanji[1], **Mingjun Zhao**[1], **Vivek J. Srinivasan**[1,2,*]

[1]Tech4Health Institute, NYU Langone Health, New York, New York 10010, USA

[2]Department of Ophthalmology, NYU Langone Health, New York, New York 10017, USA

Abstract

Dynamic multiple light scattering (DMLS) has found numerous applications, including soft matter physics and biomedical optics. Yet biological tissues may have complex internal geometries, presenting a challenge for noninvasive measurements. Deciphering laminar dynamics is crucial to accurately interpret tissue or organ physiology. Seminal DMLS work noted that one can probe deeper layers indirectly by analyzing light fluctuations on shorter time scales. Recent technologies have enabled probing deeper layers directly by analyzing fluctuations at longer path lengths. The following question arises: are the indirect and direct approaches synergistic or redundant? Here, by adding an optical switch to path-length-filtered interferometric diffusing wave spectroscopy, we experimentally address this question in the context of a forearm occlusion study. We find that both approaches afford better distinction of light scattering dynamics in layered tissues than either approach alone. This motivates further development of methods that integrate both decorrelation time scale and light path length to probe layered tissues.

In biomedical optics, dynamic multiple light scattering (DMLS) from the blood gives rise to measurable fluctuations that can provide a quantitative index of blood flow [1]. This blood flow index (BFI) is measured by coherent detection in diffuse correlation spectroscopy (DCS) [1]. While DCS can noninvasively probe deep tissues, biological tissues are layered. One major challenge for DCS is to assess a deep layer in the presence of signals from intervening tissues. Meeting this challenge requires depth specificity: high sensitivity to deeper layers and low sensitivity to more superficial layers. Even though DCS is a continuous-wave (CW) technique and, as such, provides no direct path-length information, a seminal work showed that long light paths impact coherent light fluctuations at shorter time scales [2]. Thus analyzing the field autocorrelation at early time lags is an approach, albeit indirect, to probe deeper layers. Interestingly this approach is used sparingly in the field [3,4] and sometimes with negligible effect [5,6].

A more direct and intuitive approach to probe deeper layers is to select longer tissue paths [7]. Over the years, creative approaches have been applied to resolve the path length in DMLS of suspensions [8,9]. More recently, a number of technologies have emerged to

*Vivek.Srinivasan@nyulangone.org .

directly provide the path length of coherent light fluctuations *in vivo*, including time–domain DCS [4,10,11], path-length-resolved (interferometric) DCS [12], interferometric NIRS [13], and interferometric diffusing wave spectroscopy (iDWS) with a TOF filter [14]. However, path-length-discriminated approaches are more complicated than simple CW approaches and, sometimes, photon-starved. The following questions arise: is it sufficient to use simpler CW techniques [15] and fit early decorrelation to assess deep flow [Fig. 1(a)]? Or is there a distinct benefit to detecting path-length-resolved light fluctuations [Fig. 1(b)]?

Answering these questions experimentally requires a TOF-discriminated approach with a signal-to-noise ratio to precisely measure early time scales where decorrelation is subtle. Here we employ path-length-filtered iDWS [14], which provides this set of characteristics. We realize a path-length filter by modulating the effective temporal coherence of the iDWS laser [Fig. 2]. We also introduce a pair of optical switches into the reference arm, alternating between longer paths and shorter paths at the heart rate. Critically, this system can discriminate short and long light paths quasi-simultaneously, enabling statistically powerful paired single-trial comparisons. Its many detection channels enable a high measurement SNR. To evaluate approaches to achieve depth specificity, we use a classic forearm occlusion protocol, with well-characterized laminar overshoot responses, characterized previously with continuous-wave (CW) DCS by increasing a source–collector (S–C) separation [16]. We analyze changes in BFI for long and short paths during both occlusion and hyperemic overshoot.

The iDWS system [Fig. 2(a)] utilizes path-length discrimination [14] with added optical switching to select between two reference paths. An instantaneously narrow linewidth (~10 MHz) DBR laser at 852 nm, with a sample illumination power of approximately 70 mW, is current modulated by an RF sinusoid at 9.79 MHz and user-specified (variable) peak-to-peak current. Current modulation at this frequency induces optical frequency modulation via carrier density modulation, broadening the effective power spectrum and reducing the effective temporal coherence, as modeled with a Bessel-squared TOF filter [14], which is maximized for matched sample and reference path lengths [Fig. 2(b)].

Our previous path-length-filtered iDWS [14] was able to achieve either short or long path-length selectivity, but changing the filter center required swapping reference fibers. In this work, we take the technology one step further, incorporating switches to quasi-concurrently (to within a heartbeat) measure both short and long paths. The fiber optic switches are electronically controlled micro-electromechanical (MEMS) devices, which are quasi-synchronously (switching from early to late TOFs takes ~70 ms, whereas switching from late to early TOFs takes 15 ms) operated to select either reference path P_1 (long) or P_2 (short), which differ in their respective time delays. The switchable reference paths centered the TOF filter at either late (P_1, $\tau_{S1} = 1.86$ ns) or early (P_2, $\tau_{S2} = 0.1$ ns) sample TOFs [Fig. 2(b)]. The switches transition between the two paths at approximately the heart rate, so that in successive heart beats, the system selects long paths (P_1) and then short paths (P_2). An analog output card (National Instruments) which synchronously controls both the RF signal generator and the switches such that switching reference paths is timed with RF voltages V_1 and V_2, corresponding to the optimal filter widths, Δf_1 and Δf_2, as defined below, for

each respective path. The selection of long/short photon paths is equivalent to selection of late/early TOFs, as shown on a simulated time-of-flight distribution (DTOF) of the human forearm ($\mu_a = 0.1$ cm^{-1}, $\mu_s^{'} = 7$ cm^{-1} [16]) in Fig. 2(b). The first zero of the TOF filter is $2.405/\pi \Delta f$ from the peak [Fig. 2(b)].

Are our early and late TOF filters able to achieve differential sensitivity to the skeletal muscle as hypothesized in Fig. 1(b)? For our long (short) path filter at 1 cm S–C separation, the mean/centroid of the filtered DTOF [$P(\tau_s)H(\tau_s)$] is estimated as 0.76 ns (0.18 ns), as compared to 0.25 ns for the unfiltered (CW) DTOF [$P(\tau_s)$]. Interestingly, a CW measurement at 2.7 cm (0.7 cm) achieves the same mean TOF as our late (early) TOF filter at 1 cm. Though a mean TOF is not a perfect proxy of penetration depth, it is well accepted that 2.7 cm and 0.7 cm S–C separations achieve differential sensitivity to the skeletal muscle [16], suggesting that our measurements do as well.

The correspondence between the RF voltage amplitude V and Δf is obtained through a separate fiber Mach–Zehnder interferometer (Fig. S4 in Supplement 1 [14]). The interference fringes are recorded for each voltage from 0 to 10 V_{pp}, and an algorithm that measures phase evolution by counting peaks and valleys between stationary points gives a measure of Δf. We found this method to yield a more accurate measure of the tuning range Δf than the conventional Hilbert transform method [14]. Though our algorithm indicated a nonlinear relationship between the RF voltage V and Δf, this relationship could be calibrated before the experiment.

Since our TOF-filtered approach does not provide direct access to optical path-length distribution, the optimal filter width was chosen to maximize the decay rate for the deep path (P_1) and to minimize the autocorrelation decay rate for the superficial path (P_2). These criteria are based on the premise that the magnitude of the decay rate increases with the path length [2]. Thus, for P_1 which aims for greater path lengths, the filter yielding the highest decay rate is optimal, whereas for P_2 which aims for lesser path lengths, the filter yielding the lowest decay rate is optimal. Figure 3 shows determination of the optimal filter width for long and short paths, based on the rules discussed above. For long paths [Fig. 3(a)], the optimal filter width occurred at $\Delta f_1 = 0.47$ GHz (corresponding to 1.64 ns peak to first zero of the Bessel filter), whereas for short paths [Fig. 3(c)], the optimal filter width occurred at $\Delta f_2 = 1.58$ GHz (corresponding to 0.48 ns peak to first zero of the Bessel filter). Note that the optimal filter width is subject and location dependent in general. It is instructive to examine the effects of the filter on the light intensity as well. The optimal filter width for long paths corresponds nearly, but not exactly, to the minimum of the intensity, which arises when the zero of the mainlobe of the Bessel filter lies at the peak of the DTOF [Fig. 2(b)], thus rejecting early photons. The optimal filter width for short paths corresponds to a quasi-plateau of weakly decreasing intensity (at least within the voltage limit of the RF generator). As the early filter is centered near the DTOF peak, a lower-filtered intensity indicates filter narrowing and better rejecting late photons [Fig. 2(b)].

We put the system to use in a classic forearm occlusion protocol [Fig. 4(a)], which comprised 3 states: 20 s baseline, 30 s occlusion, and 20 s release where a hyperemic peak

is observed [Fig. 4(b)]. Processing steps include: (1) parsing of the switch data in order to effectively segregate the data collected for paths P_1 or P_2 and processing them independently; (2) rolling mean subtraction, camera background removal, and pixel binning; (3) computing the interferometric autocorrelation after reference autocorrelation subtraction; (4) estimating $G_1(0)$ through appropriate fitting (double exponential fit up to 20 lags for late TOFs and quadratic fit up to 10 lags for the early TOFs to capture the curvature effectively), leading to g_1 as a function of lag for baseline (averaged over ~11 heartbeats), occlusion (averaged over ~17 heartbeats), and peak hyperemia (averaged over one heartbeat), where a heartbeat is ~0.8 s [Fig. 4(c)]; and (5) calculating the BFI relative to baseline ($rBFI$) for paths P_1 and P_2 across states.

The g_1 curves were found to be concave down at early lags. Such negative curvature is not expected for pure Brownian motion, as is typically assumed in DCS [1]. Therefore, to account for curvature at early lags, we fit g_1 to a model proposed by Carp *et al.* [17,18], which postulates an intrinsic time scale for randomization, τ_c. Fits to the semi-infinite DCS model were biased compared to this model. Specifically,

$$g_1(\tau_d) = \frac{\int P(\tau_s)H(\tau_s)e^{-\frac{1}{3}k^2 MSD(\tau_d)\tau_s\alpha\mu_s'\left(\frac{c}{n}\right)}d\tau_s}{\int P(\tau_s)H(\tau_s)d\tau_s},$$

(1)

where

$$MSD(\tau_d) = 6D_B\left[\tau_d - \tau_c\left\{1 - \exp\left(-\frac{\tau_d}{\tau_c}\right)\right\}\right].$$

(2)

Here τ_d is the autocorrelation lag time, $P(\tau_s)$ is the DTOF with $H(\tau_s)$ being the time-of-flight (τ_s) filter, and αD_B is the *BFI*. We fit for τ_c and αD_B for every g_1 curve to obtain a time course as well as for baseline (averaged ~11 heartbeats for our datasets), occlusion (averaged ~17 heartbeats), and peak hyperemia (single heartbeat). Fitting was performed over a range given by $g_1 \geq g_{1,thresh}$. This approach enables comparisons independent of the autocorrelation decay rate. *rBFI* is taken as αD_B with respect to baseline. When *rBFI* is determined with $g_{1,thresh} = 0.87$ [Fig. 4(b)], long paths show higher overshoot than the short paths. This suggests the efficacy of longer photon paths in achieving better depth sensitivity, as deeper muscle tissue shows higher overshoots [16].

The curvature of g_1 was highlighted by rescaling the τ_d-axis for short paths so that the $g_1 = 0.5$ crossing overlaps with that of long paths [Fig. 4(d)]. While the reasons for this deviation from the ideal Brownian model are beyond the study scope, empirically we can account for this downward curvature with the parameter τ_c, as mentioned above.

Figures 5(a) and 5(b) show *rBFI* during occlusion and peak overshoot, respectively, as a function of $g_{1,thresh}$, clearly demonstrating higher *rBFI* at early lags during a peak overshoot,

and the opposite trend during occlusion. Figures 5(c) and 5(d) show the *rBFI* time course for long (P_1) and short (P_2) paths, respectively. For long paths, the highest peak *rBFI* is observed for the earliest lags, whereas the opposite is true for short paths [Fig. 5(c)]. This suggests that even with a path-length filter [Fig. 2(b)], early (10–100 μs) fluctuation time scales must be accessed to probe layered tissues with better depth sensitivity.

Figure 6 shows the results of switching between short path filtering and no filtering (CW). CW and short path filtering show systematic differences [Figs. 6(a)–6(b)]. A larger overshoot in CW mode is evident in Figs. 6(c)–6(d). This result parallels Figs. 5(c) and 5(d), where longer paths show a larger overshoot.

Having established that short path filtering is beneficial, we performed 8 trials of forearm occlusion with quasi-concurrent switching between long and short paths. We fit $g_1(\tau_d)$ to Eq. (2) for different $g_{1,\text{thresh}}$ to obtain *rBFI* as a function of $g_{1,\text{thresh}}$ [Figs. 7(a) and 7(b)]. For peak hyperemic overshoot [Fig. 7(b)], *rBFI* peaks at later lags tend to be similar for both paths. When early lags are selected, however, *rBFI* for long paths exceeds that for short paths. Such differences can only be appreciated when considering different time scales (lags) and path lengths. While these results parallel those reported in [4], our work benefits from a high autocorrelation SNR afforded by >100 parallel channels, which enables higher fidelity g_1 curves to observe the effects of continuously varying fitting range. Moreover, this work is distinct in the use of a model with a physical basis [18], whereas [4] follows an empirical bi-exponential fitting approach.

An interesting additional finding in this study was the variation of τ_c. We observe that for $g_{1,\text{thresh}} = 0.87$, τ_c for long paths is always lower than that for short paths during all phases. The mean (std error) values of τ_c for long paths are 2.68 μs (0.87 μs) for baseline, 34.45 μs (8.10 μs) for occlusion, and 0.84 μs (0.08 μs) for overshoot, while for short paths, they are 10.47 μs (2.01 μs) for baseline, 69.21 μs (9.94 μs) for occlusion, and 1.79 μs (0.81 μs) for overshoot. We observe that τ_c for occlusion is higher than that for baseline, and that for peak is lower than during baseline, irrespective of the chosen paths or $g_{1,\text{thresh}}$, but it has to be noted that the τ_c values for overshoot estimated through fitting are much lower than the smallest lag measurable. Since the explanation for this behavior would entail further investigation into factors influencing the ballistic-to-diffusion regime, we refrain from analyzing τ_c in detail as it is beyond the study scope.

In conclusion, we have experimentally demonstrated the merits of applying path-length filtering and short fluctuation time scale analysis together to probe deep tissue layers, demonstrating clear-cut improvements over either approach alone. This can pave the way for the synergistic use of these techniques involving path-length resolution and short lag correlators such as TD-DCS or iNIRS to obtain better depth sensitivity in critical care neuromonitoring or transabdominal fetal oximetry applications.

Funding.

Data availability.

Data underlying the results presented in this paper are not publicly available at this time but may be obtained from the authors upon reasonable request.

REFERENCES

1. Durduran T, Choe R, Baker WB, et al., Rep. Prog. Phys 73, 076701 (2010). [PubMed: 26120204]

2. Pine DJ, Weitz DA, Chaikin PM, et al., Phys. Rev. Lett 60, 1134 (1988). [PubMed: 10037950]

3. Verdecchia K, Diop M, Lee A, et al., Biomed. Opt. Express 7, 3659 (2016). [PubMed: 27699127]

4. Samaei S, Sawosz P, Kacprzak M, et al., Sci. Rep 11, 1817 (2021). [PubMed: 33469124]

5. Wu M, Chan S-T, Mazumder D, et al., Neurophotonics 8, 015001 (2021). [PubMed: 33437846]

6. Selb J, Boas D, Chan S-T, et al., Neurophotonics 1, 015005 (2014). [PubMed: 25453036]

7. Torricelli A, Contini D, Pifferi A, et al., NeuroImage 85, 28 (2014). [PubMed: 23747285]

8. Yodh AG, Kaplan PD, and Pine DJ, Phys. Rev. B 42, 4744 (1990).

9. Bizheva KK, Siegel AM, and Boas DA, Phys. Rev. E 58, 7664 (1998).

10. Sutin JDB, Zimmerman B, Tyulmankov D, et al., Optica 3, 1006 (2016). [PubMed: 28008417]

11. Pagliazzi M, Sekar SKV, Colombo L, et al., Biomed. Opt. Express 8, 5311 (2017). [PubMed: 29188122]

12. Safi AM, Moka S, Harrah M, et al., in Biophotonics Congress 2021, OSA Technical Digest (Optica Publishing Group, 2021), p. BTh1B.6.

13. Kholiqov O, Zhou W, Zhang T, et al., Nat. Commun 11, 391 (2020). [PubMed: 31959896]

14. Zhao M, Zhou W, Aparanji S, et al., Optica 10, 42 (2023). [PubMed: 37275218]

15. Shang Y and Yu G, Appl. Phys. Lett 105, 133702 (2014). [PubMed: 25378708]

16. Yu G, Durduran T, Lech G, et al., J. Biomed. Opt 10, 024027 (2005). [PubMed: 15910100]

17. Berne BJ and Pecora R, Dynamic Light Scattering: with Applications to Chemistry, Biology, and Physics (Courier Corporation, 2000).

18. Carp SA, Roche-Labarbe N, Franceschini M-A, et al., Biomed. Opt. Express 2, 2047 (2011). [PubMed: 21750779]
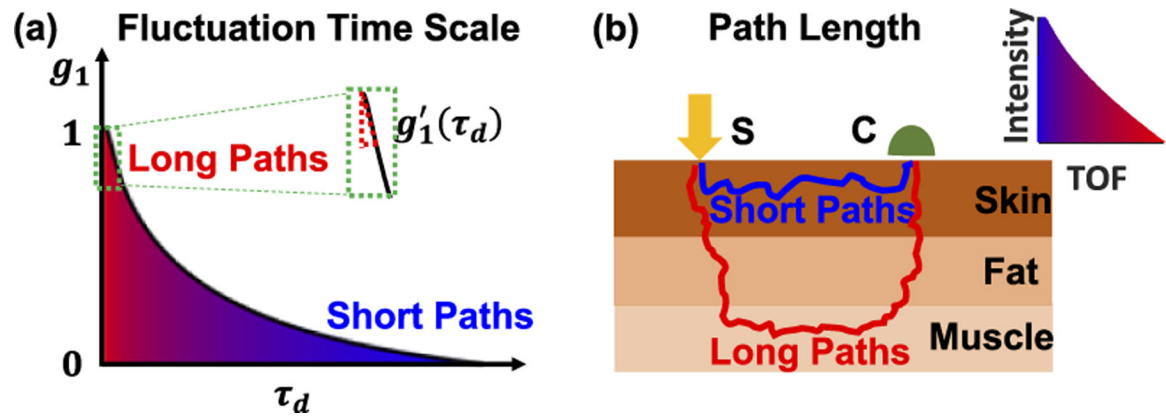
Fig. 1.

Two approaches to probe deeper layers in DMLS: (a) indirectly, by selecting early time scales in the autocorrelation, and (b) directly, by selecting longer paths. S, source; C, collector.
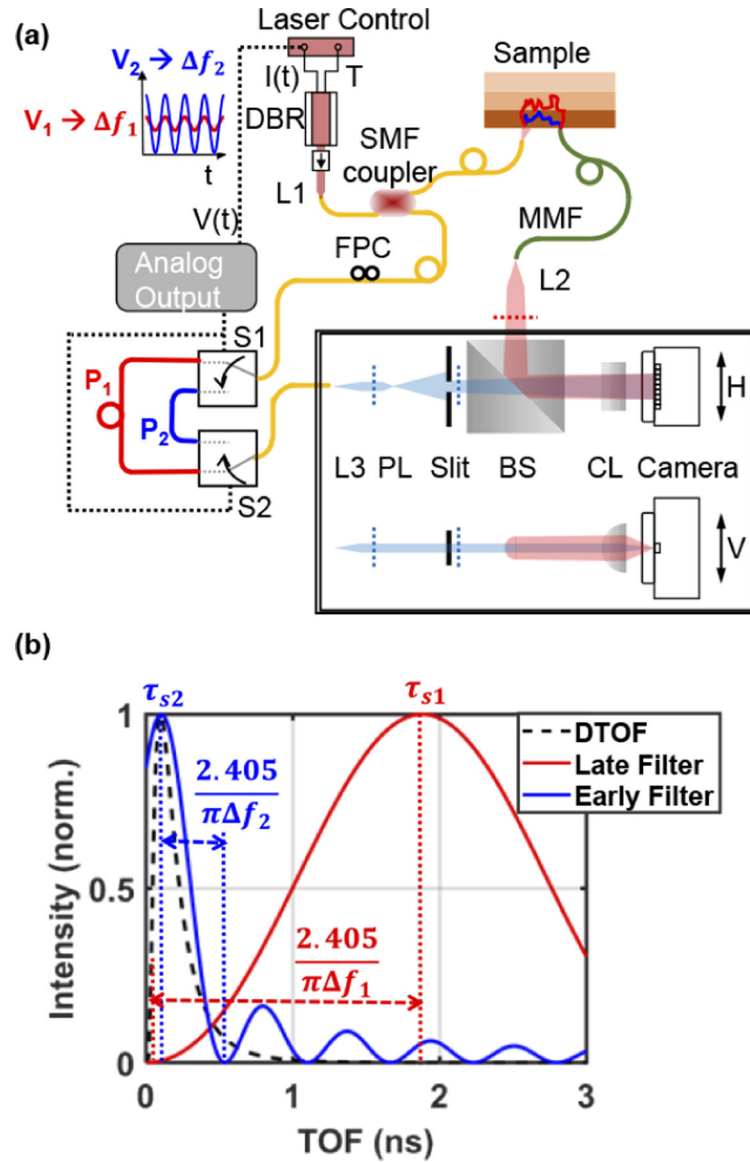
Fig. 2.
(a) Path-length-filtered iDWS setup with optical switches allows the user to electronically choose between two TOF filter centers and also specify the TOF filter width. (b) As implemented, the system selects either long or short paths corresponding to the either the late (τ_{s1}) or early (τ_{s2}) TOF filter, respectively. S1, S2: MEMS fiber switches, P_1, P_2: long and short paths.
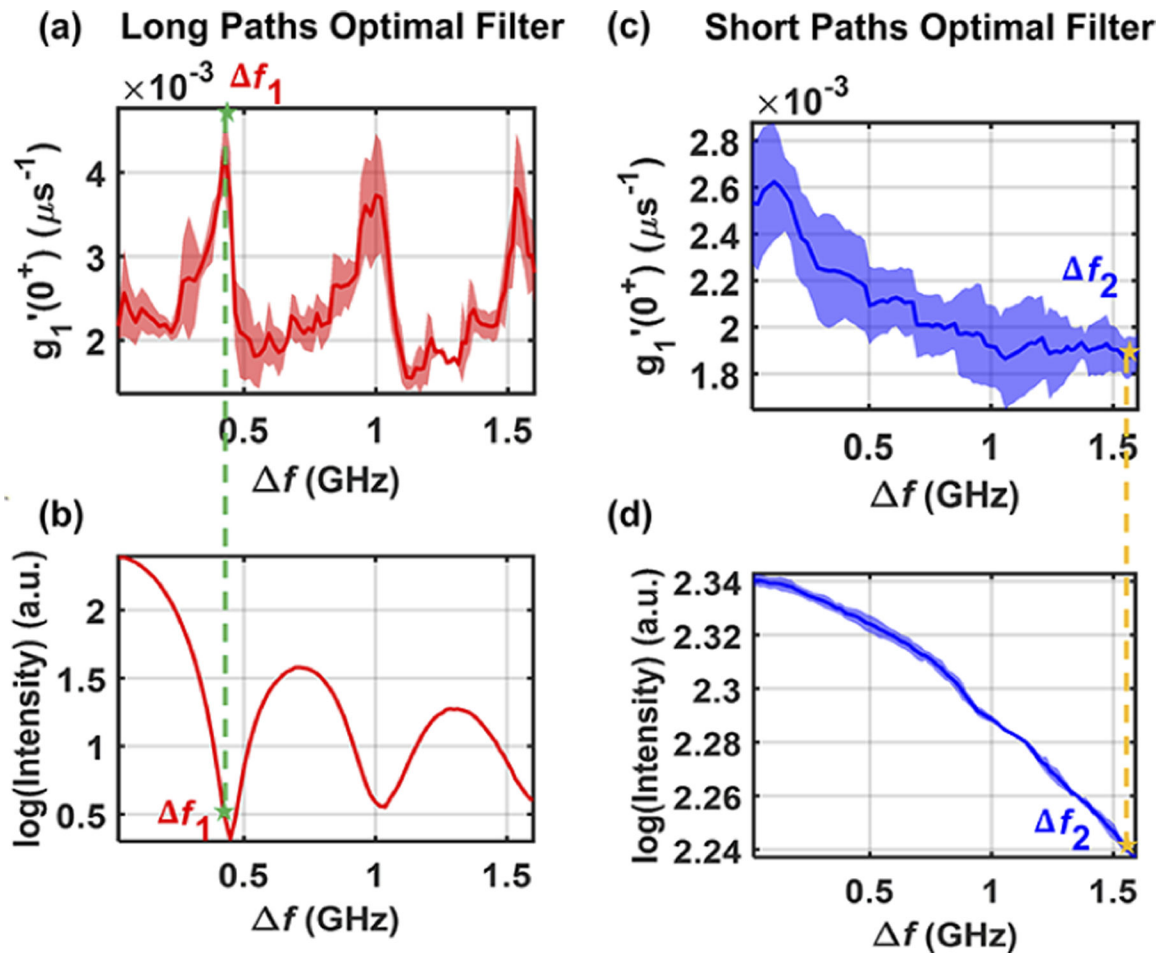
Fig. 3.
Decay rate and filtered intensity as a function of filter width, parameterized by Δf, for long [(a) and (b)] and short [(c) and (d)] paths. Optimal filter locations, defined by the criteria discussed in the text, are denoted by stars. Shading denotes standard deviation across three consecutive filter sweeps.
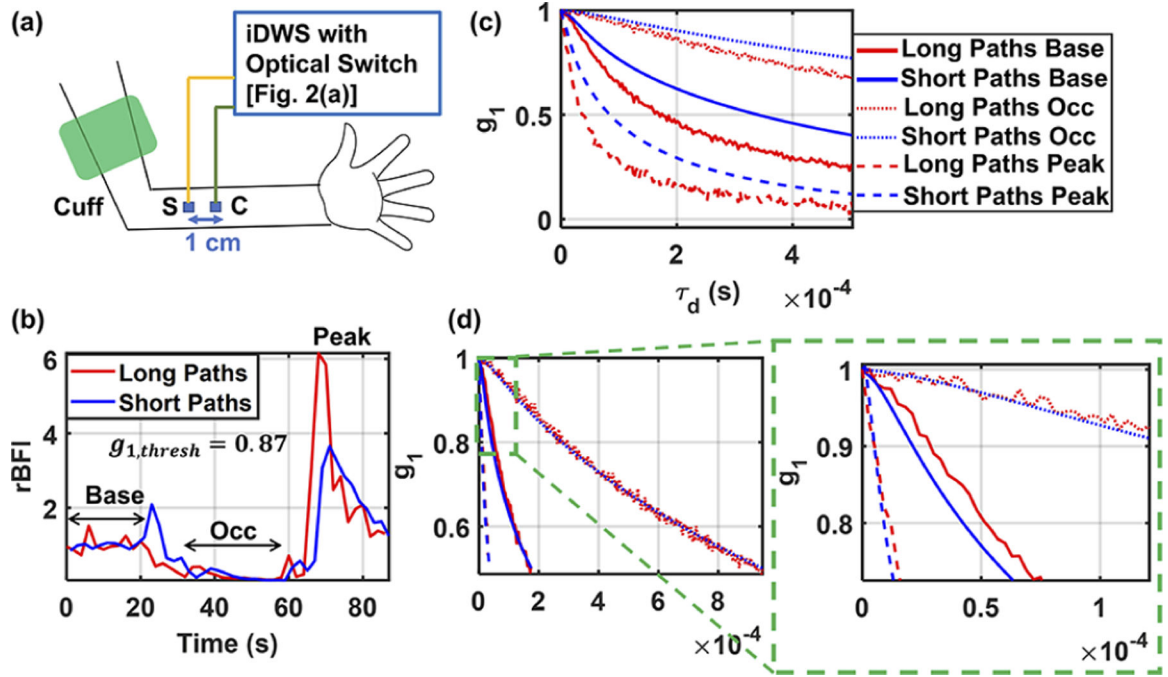
Fig. 4.

(a) Forearm occlusion protocol for system validation. (b) *BFI* relative to baseline (*rBFI*) for each path calculated for $g_{1,thresh} = 0.87$. (c) Autocorrelation (g_1) curves for long and short paths at baseline (averaged ~11 heartbeats), occlusion (averaged ~17 heartbeats), and peak overshoot (averaged single heartbeat). (d) Autocorrelation curves for long paths overlaid with rescaled short paths curves from (c) with the same legend as (c); green dotted box: zoom (S, source; C, collector).
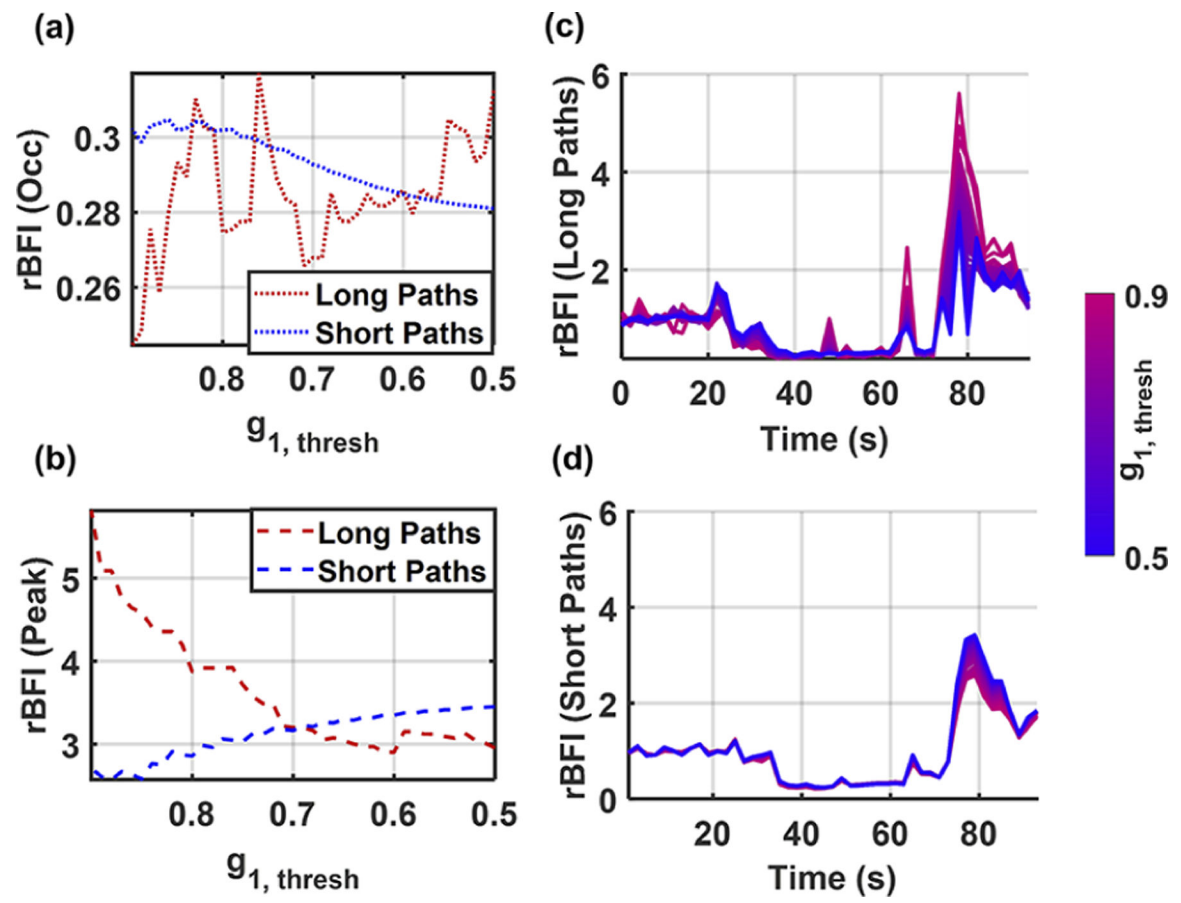
Fig. 5.

rBFI during occlusion (a) and peak overshoot (b), as a function of $g_{1,\text{thresh}}$, for both long and short paths. (c) and (d) *rBFI* time course as a function of $g_{1,\text{thresh}}$, for long paths (P_1) and short paths (P_2), respectively.
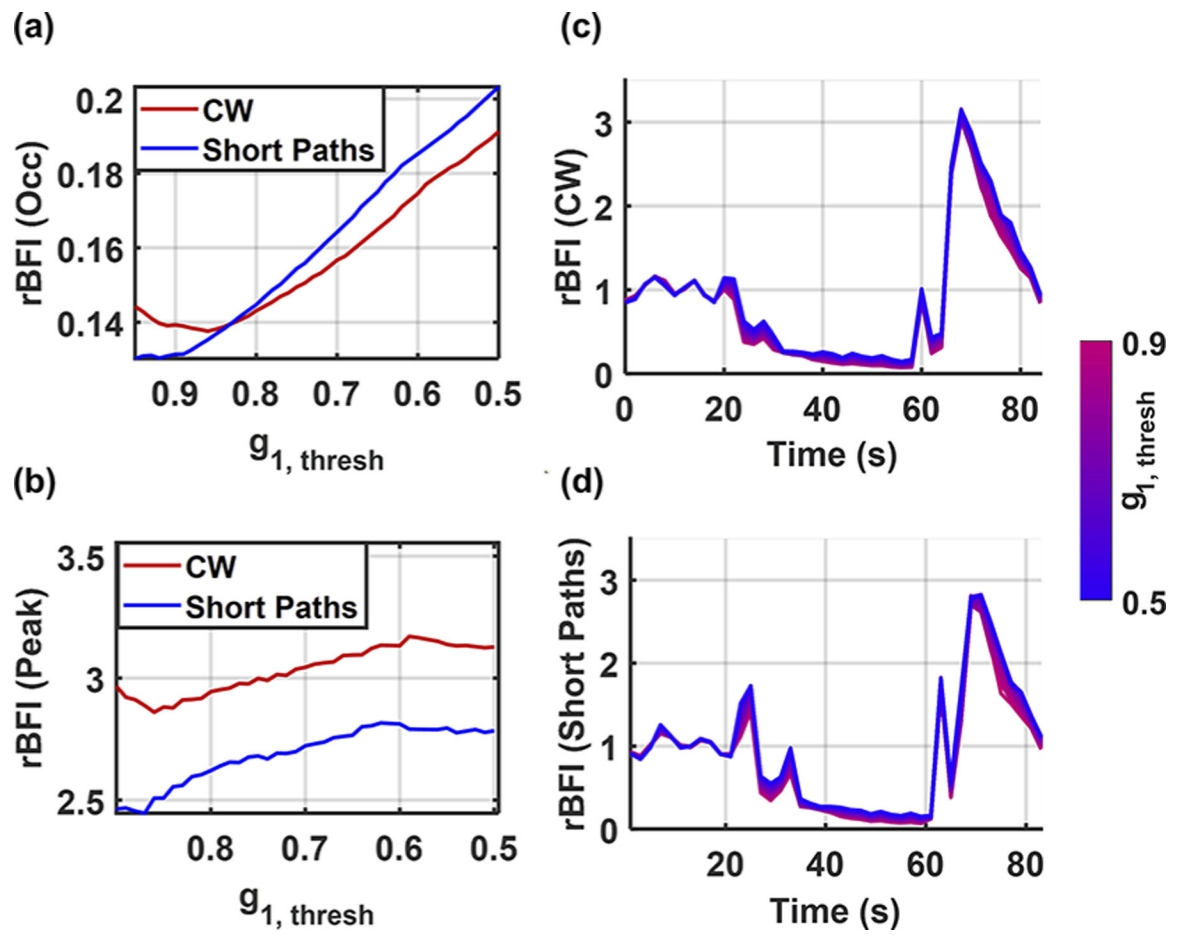
Fig. 6.

Comparison of continuous-wave (CW) and short paths. *rBFI* during occlusion (a) and peak overshoot (b), as a function of $g_{1,\,thresh}$, for both CW and short paths. (c) and (d) *rBFI* time course as a function of threshold, for CW and short paths, respectively.
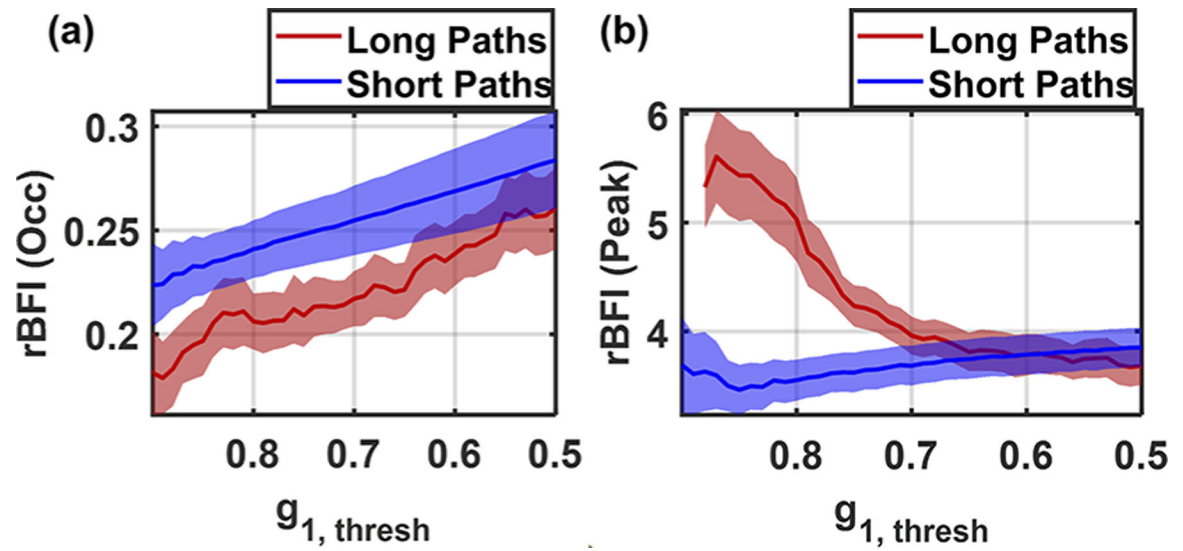
Fig. 7.
Shaded plot (mean ± std. err) summarizing *rBFI* for different g_1 thresholds for long versus short paths during occlusion (a) and peak hyperemic overshoot (b). Results show a synergistic interaction of path length and fluctuation time scale. Note that the occlusion values are averaged over a 17-heartbeat time window, and as such, do not represent the minimal observed BFI.